Explicit High-Order Discontinuous Galerkin Spectral Element Methods for LES and DNS

A. Beck, T. Bolemann, T. Hitz, V. Mayer, and C.-D. Munz

Abstract In this work we apply the high-order discontinuous Galerkin spectral element method (DGSEM) with explicit Runge-Kutta time integration to a classical square duct channel flow problem, which is a widely used benchmark case for turbulent flows. We show that due to its good scale resolving capabilities and low dispersion and dissipation errors DGSEM is a suitable alternative to both finite difference and finite volume methods in the field of LES and DNS. We demonstrate the computational efficiency and parallel scalability of the scheme by performing both DNS and LES simulations of the channel flow at a Reynolds number of $Re_\tau = 395$. We employ an implicit closure strategy for the subgrid fluxes in the LES setting and show that our results are on par with reference results from literature.

1 Introduction

Direct numerical simulation (DNS) and to a lesser extent large-eddy simulation (LES) of compressible flows are the most accurate but also most costly tools in computational fluid dynamics. They have thus mostly been applied to a range of selected problems, which could be characterized by having a rather simple geometry and low to medium Reynolds numbers, in contrast to the very complex geometries and high Reynolds regimes of RANS simulations typically used in an industrial setting. However, for LES and DNS to become affordable to a wider audience, numerical methods need to be more efficient and accurate and at the same time harness the computing power of today's parallel compute architectures. The first time DG methods appeared in literature was in the early 1970s, where Reed and Hill [30] and Lesaint and Raviart [26] applied them to neutron transport equations. In the early 1990s research interest in the field of DG arose again after a series of papers by Cockburn and Shu [12, 13], who found a DG formulation for non-linear hyperbolic systems. Several years later Bassi and Rebay extended the method for

A. Beck • T. Bolemann (✉) • T. Hitz • V. Mayer • C.-D. Munz
Institute of Aerodynamics and Gasdynamics, Pfaffenwaldring 21, 70569 Stuttgart, Germany
e-mail: beck@iag.uni-stuttgart.de; bolemann@iag.uni-stuttgart.de; hitz@iag.uni-stuttgart.de; mayer@iag.uni-stuttgart.de; munz@iag.uni-stuttgart.de

M. Mehl et al. (eds.), *Recent Trends in Computational Engineering - CE2014*,
Lecture Notes in Computational Science and Engineering 105,
DOI 10.1007/978-3-319-22997-3_17

the compressible Navier-Stokes equations [1, 3], paving the way for DG to become a practical tool in CFD. Further notable research for viscous problems has been conducted by Cockburn and Shu [14] and Warburton et al. [34].

It was also Bassi and Rebay [2] who pointed out that DG methods require a high-order boundary representation to retain their high-order of accuracy near curved boundaries. This has been identified [23] as a key problem for the industrial application of DG methods, where complex geometries are required. Since then several approaches have been proposed to generate curved meshes [17, 20].

For a long period of time DG methods for LES and DNS have only been of minor interest, research was largely focused on high Reynolds number RANS [4, 18, 28]. However, in recent years two mentionable large-scale projects [23, 24] with focus on RANS-DG found that while DG methods are more accurate per degree of freedom than existing first and second order methods, they still could only in few cases beat these state-of-the-art methods in terms of overall efficiency. This is mostly due to the large system matrices of the implicit schemes occurring for higher polynomial degrees and a lack of DG-optimized preconditioners, which are at the present time an active topic of research [7, 8].

On the other hand high-order DG has rarely been applied to LES and DNS, despite the methods superior scale resolving capabilities and highly parallel nature. In [16], Gassner and Kopriva showed that for DG methods at high polynomial degrees, while dispersion and dissipation already being very low, the remaining dissipation even exhibits a spectral cut-off like behavior, providing an accurate numerical representation over a wide range of scales. In [15], Gassner and Beck carried out under-resolved DG simulations of a homogeneous isotropic turbulent flow and could considerably outperform finite volume schemes using a de-aliased discontinuous Galerkin spectral element framework. Several other authors conclude that high-order methods are beneficial for the use in LES and DNS settings [5, 10, 29, 33] and are on par or superior to standard finite difference or finite volume methods in terms of accuracy and efficiency.

In this work we demonstrate the capabilities of our high-order explicit DGSEM-based solver *Flexi* at the example of a turbulent incompressible channel flow at a Reynolds number of $Re_\tau = 395$. For this type of channel flows extensive literature is available, we compare against the reference DNS results by Moser [27]. We first carry out a DNS to validate our framework against the reference results and followed by a "no-model" LES relying solely on the unmodified DG operator to provide sufficient numerical dissipation and on de-aliasing to prevent integration instabilities.

We start by deriving the DGSEM method for the Navier-Stokes equations in Sect. 2. In Sect. 3.1 we describe the simulation setup and present the results of the DNS and LES computations in Sect. 3.2. In Sect. 4 we briefly summarize the work carried out and discuss the results as well as potential advantages.

2 Numerical Methods

We will now briefly derive the basics of the discontinuous Galerkin spectral element method in three space dimensions. A detailed description of this particular method is available in [19], while for a general overview of DGSEM we refer to Kopriva [22]. We start by subdividing the domain $\Omega \in \mathbb{R}^d$ into non-overlapping grid-cells Q with a surface ∂Q. As DGSEM inherits the ideas from the spectral element methods, the grid cells need to support a tensor-product structure. This limits the method to quadrilateral ($d = 2$) and hexahedral ($d = 3$) elements. To recover some flexibility, the mesh can be unstructured and may also contain hanging nodes, though we will not describe the latter for simplicity.

2.1 Weak Formulation

In this work, we consider solutions to the compressible Navier-Stokes equations, which can be written as a system of conservation laws

$$U_t + \nabla_{\mathbf{x}} \cdot \mathbf{F}(U, \nabla_{\mathbf{x}} U) = 0, \quad \forall\, \mathbf{x} \in \Omega,\ t \in \mathbb{R}^+, \tag{1}$$

where $U = U(\mathbf{x}, t)$ denotes the vector of conserved quantities. The corresponding fluxes can be decomposed into $\mathbf{F} = \mathbf{F}_a(U) - \mathbf{F}_v(U, \nabla_{\mathbf{x}} U)$ with the advection component $\mathbf{F}_a$ and the viscous part $\mathbf{F}_v$. For the treatment of the solution gradients $\nabla_{\mathbf{x}} U$ we employ the BR1 scheme by Bassi and Rebay [1]. As a first step we rewrite (1) as a system of first order equations

$$\begin{aligned} U_t + \nabla_{\mathbf{x}} \cdot \mathbf{F}(U, S) &= 0, \\ S - \nabla_{\mathbf{x}} U &= 0. \end{aligned} \tag{2}$$

We now transform the equations from physical space $\mathbf{x}$ into reference space $\boldsymbol{\xi}$, with the associated inverse mapping $\mathbf{x}(\boldsymbol{\xi})$. The equations in the reference element $E = [-1, 1]^d$ read

$$\begin{aligned} J U_t + \nabla_{\boldsymbol{\xi}} \cdot \mathscr{F}(U, S) &= 0, \\ J S - \nabla_{\boldsymbol{\xi}} U &= 0 \end{aligned} \tag{3}$$

with the Jacobian $J = J(\xi)$ of the mapping and the transformed fluxes $\mathscr{F}$.

For the variational formulation we multiply by a polynomial test function $\phi(\xi)$ and integrate over the reference element

$$\begin{aligned} \int_E \left(J U_t + \nabla_{\boldsymbol{\xi}} \cdot \mathscr{F}(U, S) \right) \phi \, \mathrm{d}\xi &= 0, \\ \int_E \left(J S - \nabla_{\boldsymbol{\xi}} U \right) \phi \, \mathrm{d}\xi &= 0. \end{aligned} \tag{4}$$

We subsequently integrate by parts to split the fluxes into volume and surface contributions

$$\begin{aligned} \frac{\partial}{\partial t}\int_E JU\phi \,\mathrm{d}\xi + \oint_{\partial E} (\mathscr{F}^* \cdot \mathbf{n})\phi \,\mathrm{d}s - \int_E \mathscr{F} \cdot \left(\nabla_\xi \phi\right) \mathrm{d}\xi = 0, \\ \int_E JS\phi \,\mathrm{d}\xi + \oint_{\partial E} (U^* \cdot \mathbf{n})\phi \,\mathrm{d}s - \int_E U \cdot \left(\nabla_\xi \phi\right) \mathrm{d}\xi = 0. \end{aligned} \tag{5}$$

Here, $\mathbf{n}$ denotes the outward pointing normal vector at the element boundary and $(\mathscr{F}^*\cdot\mathbf{n})$ and $(U^*\cdot\mathbf{n})$ the fluxes and states at the boundary. In the DG setting we permit the state as well as the gradients between two elements to be discontinuous, and thus we have to define a unique value at the interface. This approximation depends on the solution on the left and right of the interface denoted by $\pm$

$$\mathscr{F}^* \cdot \mathbf{n} = \mathscr{F}_a^*(U^-, U^+) - \frac{1}{2}(\mathscr{F}_v^*(U^-, S^-) + \mathscr{F}_v^*(U^+, S^+)) \,, \tag{6}$$

$$U^* = \frac{1}{2}(U^- + U^+). \tag{7}$$

The advective part of the flux $\mathscr{F}_a^*(U^-, U^+)$ is approximated by a numerical flux function according to Roe's method [31]. The central approximation for the unique state U^* and flux $\mathscr{F}_v^*$ of the viscous part follows from the BR1 scheme [1].

For the time integration of the semi-discrete problem resulting from (5) we rely on explicit Runge-Kutta methods in various low-storage formats. For the present simulations the well-known 5-stage fourth order Williamson type scheme by Carpenter et al. [9] is used.

2.2 Numerical Approximation

As a next step we approximate the solution, its gradients and the fluxes by a tensor-product basis of 1D Lagrange polynomials $\ell(\xi)$

$$\begin{aligned} U(\boldsymbol{\xi}, t) &= \sum_{i,j,k=0}^{N} \hat{U}_{ijk}\psi_{ijk}^N(\boldsymbol{\xi}), \quad \psi_{ijk}^N(\boldsymbol{\xi}) = \ell_i^N(\xi^1)\ell_j^N(\xi^2)\ell_k^N(\xi^3), \\ \mathscr{F}^d(\boldsymbol{\xi}, t) &= \sum_{i,j,k=0}^{M} \hat{\mathscr{F}}_{ijk}^d\psi_{ijk}^M(\boldsymbol{\xi}), \quad S^d(\boldsymbol{\xi}, t) = \sum_{i,j,k=0}^{N} \hat{S}_{ijk}^d\psi_{ijk}^N(\boldsymbol{\xi}), \quad d = 1, 2, 3 \end{aligned} \tag{8}$$

with the nodal degrees of freedom $\hat{U}_{ijk}, \hat{\mathscr{F}}_{ijk}^d, \hat{S}_{ijk}^d$. Note that due to the non-linearity of the fluxes with respect to the solution, we want to use a higher polynomial degree

M to represent these, while we employ degree N for the solution as well as the gradients, with $M \geq N$.

For evaluating the integrals in (5) we rely on Legendre-Gauß quadrature. Following the Galerkin ansatz we choose the test functions $\boldsymbol{\phi(\xi)}$ to be identical to the basis functions $\ell(\xi)$. By collocating the quadrature points and interpolation points we can write the volume integral as

$$\int_E \mathscr{F}^d(U, \nabla_x U) \frac{\partial \phi}{\partial \xi^d} \, \mathrm{d}\boldsymbol{\xi} \approx \sum_{l,m,n=0}^{M} \sum_{i,j,k=0}^{M} \hat{\mathscr{F}}^l_{ijk} \psi^M_{ijk}(\boldsymbol{\xi}^M_{lmn}) \frac{\partial \phi}{\partial \xi^d} \bigg|_{\boldsymbol{\xi}=\boldsymbol{\xi}_{pqr}} \omega^M_p \omega^M_q \omega^M_r$$

$$= \sum_{l,m,n=0}^{M} \hat{\mathscr{F}}^d_{lmn} \frac{\partial \phi}{\partial \xi^d} \bigg|_{\boldsymbol{\xi}=\boldsymbol{\xi}_{pqr}} \omega^M_l \omega^M_m \omega^M_n \,, \tag{9}$$

$$\int_E S^d(U) \frac{\partial \phi}{\partial \xi^d} \, \mathrm{d}\boldsymbol{\xi} \approx \sum_{l,m,n=0}^{N} \hat{S}^d_{lmn} \frac{\partial \phi}{\partial \xi^d} \bigg|_{\boldsymbol{\xi}=\boldsymbol{\xi}_{pqr}} \omega^N_l \omega^N_m \omega^N_n \,, \tag{10}$$

where ω denotes the integration weights.

As the fluxes depend nonlinearly on the solution, they are of degree $2N$ in the incompressible and $3N$ in the compressible case and can thus be integrated exactly with $M = \frac{3}{2}N$ and $M = 2N$ following the Legendre-Gauß quadrature rule. The error resulting from a lack of integration accuracy is referred to as aliasing and can severely degrade the solution quality and introduce instabilities. We therefore refer to the process of exactly integrating the fluxes as polynomial de-aliasing. The de-aliasing not only increases accuracy but also leads to an improved robustness of the numerical scheme as a side effect. On first sight the idea of polynomial de-aliasing increases the schemes complexity and seemingly sabotages the benefits of collocation due to the different polynomial degrees of the solution and the fluxes. However, this is not the case, as the de-aliasing can be implemented efficiently by the means of a modal cutoff filter. Instead of choosing two different polynomial degrees we start with a standard DGSEM scheme using polynomial degree M and equally represent the solution U on $M + 1$ Gauß-Legendre quadrature points. We define a modal cutoff filter

$$\sigma_j = \begin{cases} 1 & j \in [1, N] \\ 0 & j \in [N+1, M] \end{cases} \tag{11}$$

where σ_j are the coefficients of the filter matrix and apply this filter to the modal represent of U each time it is updated, i.e. after every Runge-Kutta stage. This guarantees U staying a polynomial of degree N, while all integrals are evaluated on $M + 1$ points.

3 Turbulent Channel Flow

A direct numerical simulation (DNS) of a generic turbulent channel flow between two plane-parallel walls has been conducted. Furthermore, to illustrate the performance of the DGSEM for under-resolved computations, large-eddy simulations on various meshes have been conducted.

Extensive DNS data is available from Moser et al. [27] for a variety of Reynolds numbers. These test cases have often been used for LES. In 2000, Lenormand et al. [25] simulated compressible flows for Mach numbers $Ma = 0.5$ and $Ma = 1.5$, using a fourth order finite difference method and explicit SGS modelling with the Smagorinsky model and a variation of a mixed-scale model. A high order Chebyshev multi-domain staggered-grid method with polynomial degrees of $N = 6$ and $N = 10$ has been used for under-resolved DNS of a subsonic channel flow at $Ma = 0.4$ by Jacobs et al. [21] in 2005. An explicit LES of the same channel flow has been conducted by Sengupta et al. [32], using a high order spectral multi-domain method with the dynamic Smagorinsky model. More recently, Carton de Wiart et al. [11] successfully tested a fourth order DG scheme for under-resolved DNS of the channel flow at a friction Reynolds number $Re_\tau = 395$, based on the friction velocity u_τ which is linked to the averaged wall shear stress, $u_\tau = \sqrt{\tau_w/\rho}$. A further DG investigation of this problem has been carried out by Wei et al. [35] who performed direct numerical simulations at $Re_\tau = 180, 186, 208$ with the corresponding Mach numbers $Ma = 0.2, 0.7, 1.5$ at $N = 9$ applying over-integration to prevent aliasing similar to our strategy.

3.1 Simulation Setup

The numerical setup follows the DNS performed in [27] for the case with $Re_\tau = 395$. The flow features high *Re*-effects but the Reynolds number is low enough to keep the computational costs manageable. The geometry is chosen as two plane-parallel walls with Dirichlet type, isothermal, no-slip boundary conditions (BC), where the velocity at the wall is zero and the temperature is constant while in streamwise and spanwise directions periodic BC are applied. Figure 1 shows the channel with mean flow direction and BC. The dimension of the domain is chosen

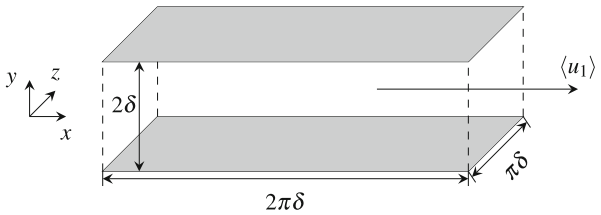

Fig. 1 Geometry of the channel with mean flow direction. The *filled grey walls* are equipped with Navier-Stokes boundary conditions. The other boundary conditions are set as periodic

as $2\pi\delta \times \pi\delta \times 2\delta$ in x, y, z directions, where x, y, z denote the streamwise, wall-normal and spanwise directions.

The geometry is simple and due to the periodic BC it resembles two planes that are infinite in streamwise and spanwise directions. This allows for the development of homogeneous turbulence in both directions, while in wall normal direction turbulence is anisotropic and near-wall effects can be studied.

Due to the streamwise periodic BC, a forcing term has to be applied to supply a pressure gradient. The formulation is taken from Benocci and Pinelli [6], using a time dependent body force that maintains a constant mass flow rate.

The grid parameters for the DNS are chosen to capture all flow phenomenas for Mach number of 0.1 which is corresponding to the reference of Moser et al. [27]. The resulting non-dimensional length scales alongside the number of elements are listed in Table 1. Here Δy_c^+ gives the y-resolution at the center line. The polynomial degree of the solution is $N = 5$ resulting in $83.1 \cdot 10^6$ degrees of freedom.

For the LES, three different grids are used, where the polynomial degree of the solution remains constant, $N = 7$, and the number of elements is varied to investigate h-convergence. We apply an incomplete polynomial de-aliasing strategy detailed in Sect. 2.2 with two de-aliased modes ($M = 9$) as opposed to the four modes required for complete de-aliasing. The three grids considered contain $35 \times 12 \times 18$, $20 \times 17 \times 17$ and $12 \times 17 \times 8$ elements in x, y, z-directions. This results in $3.87 \cdot 10^6$, $2.95 \cdot 10^6$ and $0.84 \cdot 10^6$ degrees of freedom, which is significantly less than in the DNS case. While the first case is best resolved in stream- and spanwise direction, the second and third case are better resolved in wall-normal direction though having less degrees of freedoms. The meshes are displayed in Fig. 2.

In contrast to the DNS and the simulation performed by Moser et al. [27], we choose a Mach number $Ma = 0.4$ for the LES to obtain larger convection dominated time steps. It was found that the flow field shows only negligibly small signs of compressibility.

For initialization of the LES, an asymmetric velocity profile is chosen instead of a laminar velocity profile used for the DNS. Though non-physical, the new approach

Table 1 Grid and geometry parameters of the direct numerical simulation

Re_τ	$Cells: N_x \times N_y \times N_z$	Δx^+	Δy_c^+	Δz^+
395	$86 \times 66 \times 64$	4.70	3.82	3.12

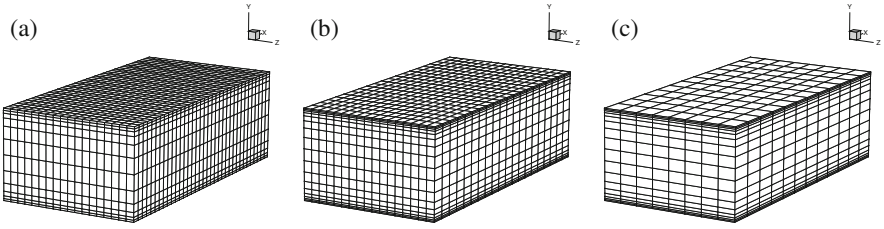

Fig. 2 Meshes of the channel geometry. (**a**) $35 \times 12 \times 18$, (**b**) $20 \times 17 \times 17$, (**c**) $12 \times 17 \times 8$

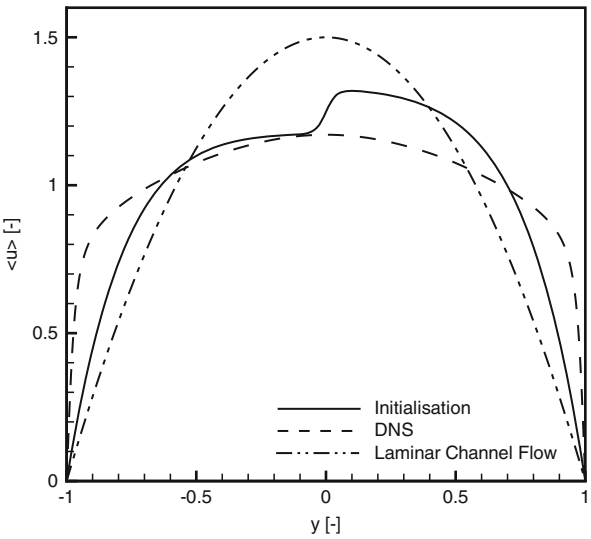

Fig. 3 Initialization of channel flow with a polynomial, superimposed by a tanh-function, a laminar velocity profile and the fully turbulent profile from [27]

yields a quicker transition to turbulence and thus reduces computation time. We did not thoroughly investigate its influence on the solution, instead we rely on a sufficiently large time-averaging period to make up for eventual side effects. A polynomial is interpolated to fit the velocity gradient at the wall and the maximum velocity at mid channel. It was then superimposed by a tanh function to obtain an inflection point at $y = 0$:

$$u(t=0) = -0.5y^6 - 0.5476y^4 - 0.2y^2 + 1.2476 + 0.075 \tanh(25y)(1-y^2). \quad (12)$$

The velocity profile is shown in Fig. 3, compared to the fully turbulent profile from [27] and the laminar velocity profile. The mean value for all three profiles is identical, resulting in the same mass flow and contained energy. Finally, random fluctuations f_{fluc} are added to all initialization profiles.

3.2 *Results for DNS and LES*

An impression of wall-bounded turbulence is given in Fig. 4, where we visualize the coherent structures of the DNS results, using the λ_2 vortex detection criterion.

The following paragraphs set out to address the DNS computation. Figure 5 (left) shows the averaged velocity profile normalized by the friction velocity in wall-coordinates $u^+ = \langle U \rangle / u_\tau$ and $y^+ = y\, u_\tau / \nu$. The results obtained by DGSEM are in very good agreement with the reference DNS. The velocity variance $\langle u_1 u_1 \rangle$ shows a slight difference above $y^+ = 75$, as presented in Fig. 5 (right).

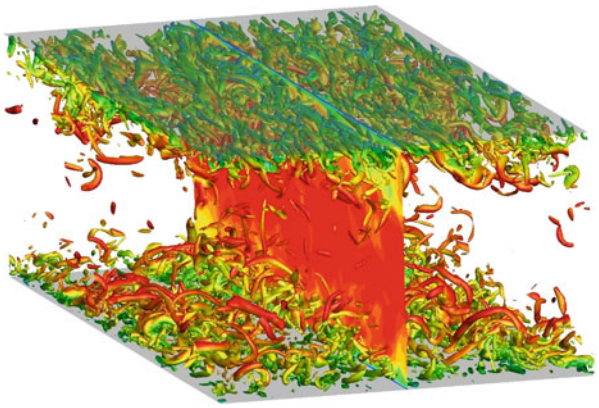

Fig. 4 λ_2-isosurfaces colored by streamwise velocity

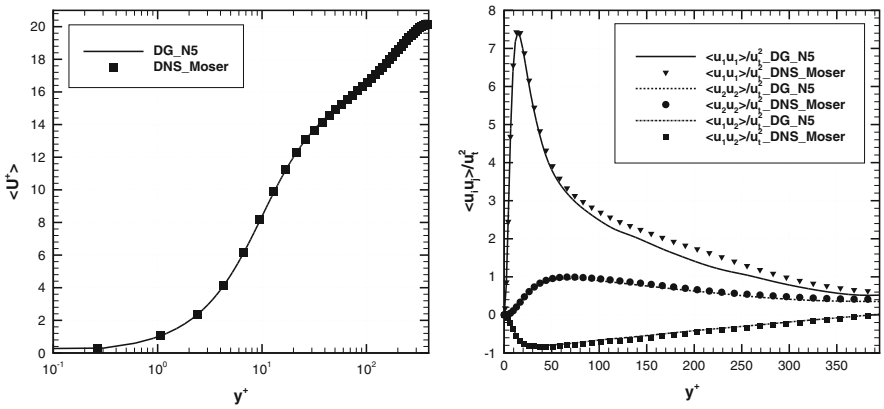

Fig. 5 Time- and spanwise-averaged velocity profile (*left*) and velocity fluctuations $u_i u_j / u_\tau$ (*right*) in wall units

A possible cause for this deviation may be an insufficient time averaging period. On the other hand, the velocity variance $\langle u_2 u_2 \rangle$ and covariance Reynolds shear stress $\langle u_1 u_2 \rangle$ are almost perfectly superimposed on the reference data. One further expected characteristic of a wall bounded flow is that the production and dissipation of turbulent kinetic energy (TKE) will be approximately in balance inside the logarithmic region. However the results also confirm the observation by Moser et al. [27] that the ratio is slowly increasing over the log range, as shown in Fig. 6. Despite the small oscillations in the balance region, the profile is well captured. Details of computational cost of the DNS are summarized in Table 2, where the characteristic time $T^* = \delta / u_b$ is chosen in relation to the characteristic length scale δ and the streamwise bulk velocity u_b.

We now discuss the results of the large-eddy simulation. Since a newly developed velocity profile has been used for initialization, the temporal development of the

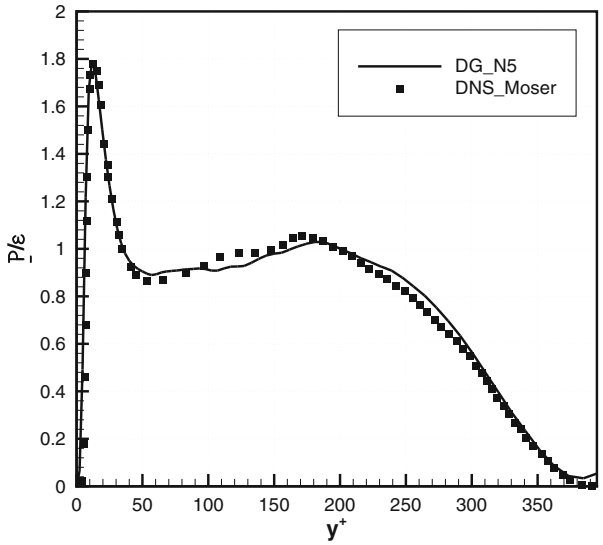

Fig. 6 Production (P) to dissipation (ϵ) ratio of TKE in wall units

Table 2 Computational setup and cost of the direct numerical simulation

Case	DOFs	$\Delta t/T^*$	Cores	Cells/core	T_{CPU}/T^*[h]	T_{run}/T^*[min]
$N = 5$	$83.1 \cdot 10^6$	$3.1 \cdot 10^{-4}$	8196	47	702	5.2

flow during the transient stage is depicted in Fig. 7 in terms of the streamwise force. After initialization, the simulation oscillates mildly due to the initial velocity fluctuations. For $t > 40$, the fluctuations are damped while the mean force in streamwise direction is slightly decreasing. Due to the non-physical velocity profile at $t = 0$, the flow solution obtained in this region is referred to as quasi-laminar flow.

Eventually, each simulation reaches the transitional regime, indicated as the rapid increase in streamwise force, representing the increased pressure gradient due to larger friction induced by turbulent wall shear stresses. Here the second case with the best wall-normal resolution is the first to make the transition at $t \approx 110$, while for both other cases transition occurs considerably later at roughly $t \approx 170$. Interestingly, these other cases show fluctuations during transition when the force in streamwise direction is near 0.08; this behaviour cannot be observed for $20 \times 17 \times 17$. As the turbulent regime is reached, each simulation settles for a mean force of approximately 0.130–0.132, while fluctuating with an amplitude up to approximately 0.01. This state is kept for the remainder of the simulation, with some perturbations of larger scale but without visible periodicity.

Turbulence statistics have been obtained by time averaging over a period of $\Delta t = 100\, u_b/\delta$, corresponding to approximately 16 flow-throughs. The characteristic parameters, or wall units, for inner scaling, wall shear stress τ_w and friction velocity

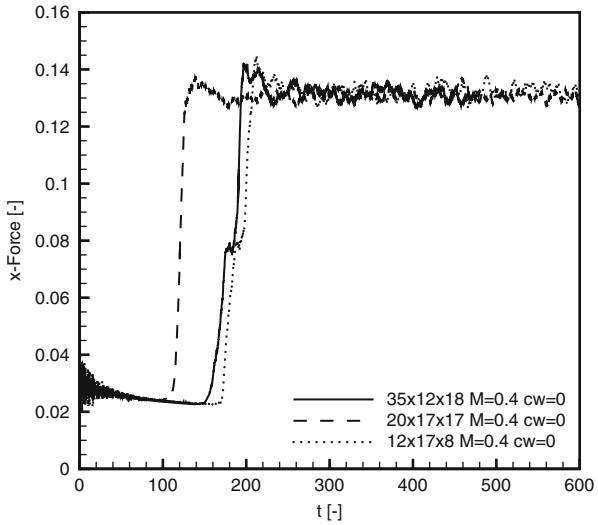

Fig. 7 Temporal development of the force in streamwise direction

Table 3 Overview over turbulent parameters for the LES calculations, compared to the DNS results from Moser et al. [27]

	$35 \times 12 \times 18$	$20 \times 17 \times 17$	$12 \times 17 \times 8$	DNS [27]
Re_τ [-]	392.09	391.52	394.03	392.24
τ_w [-]	3.322×10^{-3}	3.312×10^{-3}	3.355×10^{-3}	3.325×10^{-3}
u_τ [-]	5.764×10^{-2}	5.755×10^{-3}	5.792×10^{-2}	5.766×10^{-2}
u_c [-]	1.146	1.152	1.155	1.161
y_1^+, cell [-]	17.54	8.54	8.64	–

u_τ, are calculated as averaged mean values over both channel walls. An overview over these parameters, Re_τ and the velocity at the channel centre u_c is given in Table 3 along with the spatial resolution in wall units. Case $35 \times 12 \times 17$, with $Re_\tau = 392.09$, comes very close to the DNS value, whereas the coarser grid $20 \times 17 \times 17$ further underestimates it with $Re_\tau = 391.52$ and the coarsest grid overestimates it with $Re_\tau = 394.03$. Both τ_w and u_τ behave similarly. More interestingly, the center-line velocity u_c comes closest for the coarse mesh, the relative error compared to Moser et al. [27] is only 0.53 %, while for $35 \times 12 \times 18$ it is underestimated by 1.26 %.

For profiles of mean velocities and Reynolds stresses, the statistics are averaged in both homogeneous directions, yielding profiles varying only in wall-normal direction y. For visualization, the solution is interpolated on a grid with $N_{Visu} = 20$ interpolation points, equidistantly distributed in each element.

For each mesh, the streamwise mean velocity is very close to the DNS by Moser et al. [27]. At the wall, all simulations are identical and meet the correct gradients.

Only from the buffer region at $y^+ > 10$ they deviate. At the beginning of the log-layer, at $y^+ \approx 12$, they all underestimate the DNS. This can be attributed to the underestimation of centre velocity u_c, however, $12 \times 17 \times 8$ features also an overestimation in friction velocity while u_c is larger than for the other cases. Both effects contribute to the behavior of mean velocity u^+. The largest deviation from the DNS is reached by $12 \times 17 \times 8$ in the buffer layer and by both $35 \times 12 \times 18$ and $12 \times 17 \times 8$ at the channel center-line. Furthermore, at those locations, the deviation between the DGSEM results themselves is most distinctive. As a measure of accuracy, the relative $\mathbb{L}_2$-error norm, normalized by the $\mathbb{L}_2$-norm of the solution by Moser et al. [27], and the $\mathbb{L}_\infty$-error has been calculated. Both yield best results for $20 \times 17 \times 17$ with $\mathbb{L}_2(u^+) = 1.147 \times 10^{-2}$ and $\mathbb{L}_\infty(u^+) = 2.535 \times 10^{-1}$ (Fig. 8).

The more challenging profiles of Reynolds stresses $\langle u_i' u_j' \rangle$ are plotted as functions of the wall distance in Fig. 9a–d. $(\cdot)^+$ indicates a representation in wall units, i.e. the stresses are normalized by u_τ^2. The shear stresses $(u'w')^+$ and $(v'w')^+$ are theoretically zero and are therefore omitted in the figure.

The general observation for all Reynolds stresses is that the fine grid predicts the solutions closest to the DNS values. Especially at the wall, except for the spanwise stress $(w'w')^+$, all simulations reproduce the gradients exactly, including the accurate location of the peak values. The spanwise stress, however, shows a larger deviation for the coarsest mesh which is attributed to inferior spatial resolution in the spanwise direction.

The streamwise normal stress in Fig. 9 is underestimated for every mesh. Especially the small peak value is in literature often considered an indication of

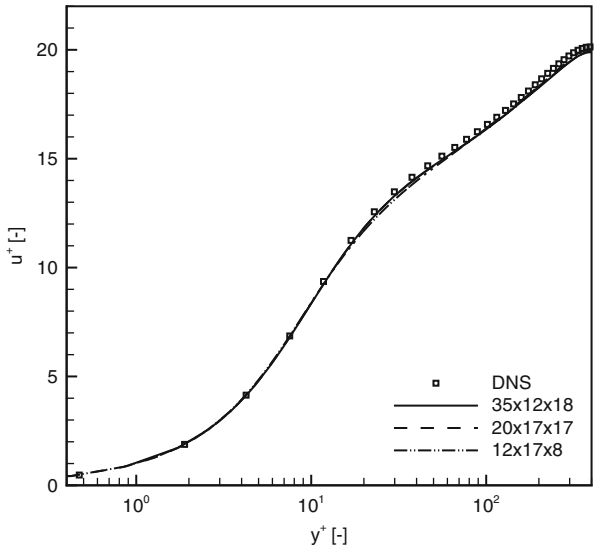

Fig. 8 u^+ in logarithmic-normal representation, plotted over y^+ for different meshes. DNS for comparison is taken from [27]

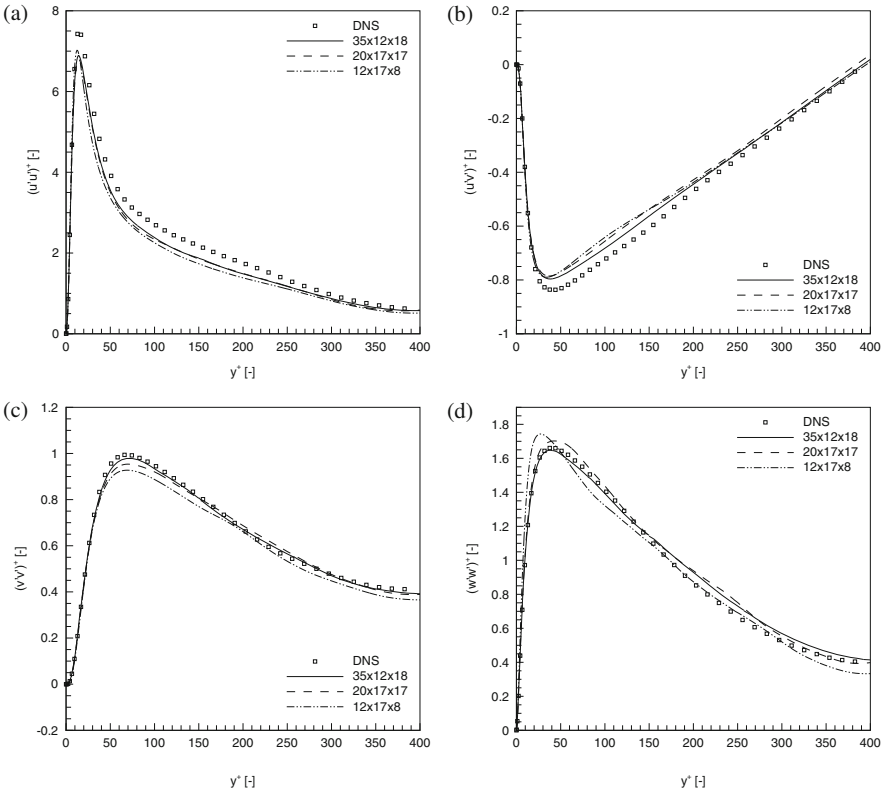

Fig. 9 Reynold stresses (**a**) $(u'u')^+$, (**b**) $(u'v')^+$, (**c**) $(v'v')^+$, (**d**) $(w'w')^+$ in normal-normal representation. Each profile is plotted over y^+. DNS for comparison is taken from [27]

under dissipative behavior [21, 25]. This assumption is supported by the fact that the coarsest simulation, which is expected to be the most dissipative one, reaches the maximum slightly closer to the wall and with a larger magnitude. However, the results for the streamwise normal stress deviate only little from each other, the same accounts for the shear stress $(u'v')^+$, displayed in Fig. 9b.

A general trend, regarding the solution quality of the remaining Reynolds stresses depending on the h-resolution is found only close to the wall. There, the wall normal stress $(v'v')^+$ (Fig. 9c) reduces its magnitude for coarser meshes, while the spanwise stress $(w'w')^+$ (Fig. 9d) predicts the opposite behavior.

In conclusion, $35\times12\times18$ produces the best results, caused by its superior spatial resolution in spanwise and streamwise directions. As expected, the largest errors occur with the coarse mesh but, nevertheless, the solution is still close to the DNS, although there is no explicit SGS model active. The results of the LES, or under-resolved DNS, indicate that the high-order approximation is capable of resolving a large range of scales, while the polynomial de-aliasing provides stability and the numerical dissipation accounts for the subgrid effects.

4 Conclusion

In this work, we have demonstrated that high-order discontinuous Galerkin methods are inherently well suited for the simulation of turbulent flows at moderate Reynolds numbers. We have chosen a well investigated square duct channel flow at $Re_\tau = 395$ as a benchmark case and carried out a direct numerical simulation as well as a "no-model" large-eddy simulation, where we do not use any explicit or implicit subgrid scale model. For the LES we apply incomplete de-aliasing to greatly reduce integration errors and render our simulations accurate and stable. We show that for both the DNS and the LES our results are in good agreement with the reference results from literature, despite the LES having significantly less degrees of freedom then both DNS. Due to the schemes excellent parallel scalability several thousand cores could be used for the DNS with $83 \cdot 10^6$ DOFs. Unlike finite difference schemes our numerical framework is fully unstructured and can be applied to more complex flows and geometries in a straight-forward fashion. We conclude that DG methods are favorable for scale-resolving simulations and are capable of delivering high-fidelity results not only in well-resolved but also in under-resolved settings, for moderate Reynolds numbers even without a necessity for explicit subgrid scale modeling.

Acknowledgement The authors would like to thank the Höchstleistungsrechenzentrum Stuttgart (HLRS) for providing the computational resources for this work in the context of the *hpcdg* project.

References

1. Bassi, F., Rebay, S.: A high order accurate discontinuous finite element method for the numerical solution of the compressible Navier–Stokes equations. J. Comput. Phys. **131**, 267–279 (1997)
2. Bassi, F., Rebay, S.: A high-order discontinuous Galerkin finite element method solution of the 2d Euler equations. J. Comput. Phys. **138**, 251–285 (1997)
3. Bassi, F., Rebay, S.: Numerical evaluation of two discontinuous Galerkin methods for the compressible Navier–Stokes equations. Int. J. Numer. Methods Fluids **40**(1–2), 197–207 (2002)
4. Bassi, F., Crivellini, A., Rebay, S., Savini, M.: Discontinuous Galerkin solution of the Reynolds-averaged Navier–Stokes and k-ω turbulence model equations. Comput. Fluids **34**(4–5), 507–540 (2005)
5. Beck, A.D., Bolemann, T., Flad, D., Frank, H., Gassner, G.J., Hindenlang, F., Munz, C.D.: High-order discontinuous Galerkin spectral element methods for transitional and turbulent flow simulations. Int. J. Numer. Methods Fluids **76**(8), 522–548 (2014)
6. Benocci, C., Pinelli, A.: Engineering turbulence modelling and experiments. In: Proceedings of the International Symposium on Engineering Turbulence Modelling and Measurements. Elsevier Science Ltd, Amsterdam (1990)
7. Birken, P., Gassner, G., Haas, M., Munz, C.D.: Preconditioning for modal discontinuous Galerkin methods for unsteady 3D Navier–Stokes equations. J. Comput. Phys. **240**, 20–35 (2013)

8. Brix, K., Pinto, M.C., Canuto, C., Dahmen, W.: Multilevel preconditioning of discontinuous Galerkin spectral element methods. Part I: geometrically conforming meshes. IMA J. Numer. Anal. (2014) http://imajna.oxfordjournals.org/content/early/2014/12/02/imanum.dru053.abstract
9. Carpenter, M., Kennedy, C.: Fourth-order 2N-storage Runge-Kutta schemes. Technical Report, NASA TM 109111 (1994)
10. Carton de Wiart, C., Hillewaert, K.: DNS and ILES of transitional flows around a SD7003 using a high order discontinuous Galerkin method. In: Seventh International Conference on Computational Fluid Dynamics (ICCFD7) (2012)
11. Carton de Wiart, C., Hillewaert, K., Geuzaine, P., Luccioni, R., Bricteux, L., Coussement, G., Winckelmans, G.: Assessment of LES modeling within a high order discontinuous Galerkin solver. In: Proceedings of 9th International ERCOFTAC Symposium on Engineering Turbulence Modelling and Measurements (2012)
12. Cockburn, B., Shu, C.W.: TVB Runge-Kutta local projection discontinuous Galerkin finite element method for conservation laws II: general framework. Math. Comput. **52**, 411–435 (1989)
13. Cockburn, B., Shu, C.W.: The Runge-Kutta local projection p1-discontinuous Galerkin finite element method for scalar conservation laws. RAIRO Modél. Math. Anal. Numér **25**(3), 337–361 (1991)
14. Cockburn, B., Shu, C.W.: The local discontinuous Galerkin method for time-dependent convection diffusion systems. SIAM J. Numer. Anal. **35**(6), 2440–2463 (1998)
15. Gassner, G., Beck, A.: On the accuracy of high-order discretizations for underresolved turbulence simulations. Theor. Comput. Fluid Dyn. **27**(3–4), 221–237 (2013)
16. Gassner, G., Kopriva, D.: A comparison of the dispersion and dissipation errors of Gauss and Gauss-Lobatto discontinuous Galerkin spectral element methods. SIAM J. Sci. Comput. **33**(5), 2560–2579 (2011)
17. Geuzaine, C., Remacle, J.F.: Gmsh: A 3-d finite element mesh generator with built-in pre-and post-processing facilities. Int. J. Numer. Methods Eng. **79**(11), 1309–1331 (2009)
18. Hartmann, R., Held, J., Leicht, T.: Adjoint-based error estimation and adaptive mesh refinement for the rans and k–ω turbulence model equations. J. Comput. Phys. **230**(11), 4268–4284 (2011)
19. Hindenlang, F., Gassner, G.J., Altmann, C., Beck, A., Staudenmaier, M., Munz, C.D.: Explicit discontinuous Galerkin methods for unsteady problems. Comput. Fluids **61**, 86–93 (2012)
20. Hindenlang, F., Bolemann, T., Munz, C.D.: Mesh curving techniques for high order discontinuous Galerkin simulations. In: IDIHOM: Industrialization of High-Order Methods-A Top-Down Approach, pp. 133–152. Springer, Berlin (2015)
21. Jacobs, G., Kopriva, D., Mashayek, F.: Validation study of a multidomain spectral code for simulation of turbulent flows. AIAA J. **43**, 1256–1264 (2005)
22. Kopriva, D.A.: Implementing Spectral Methods for Partial Differential Equations. Algorithms for Scientists and Engineers, 1st edn. Springer Science & Business Media, New York (2009)
23. Kroll, N., Bieler, H., Deconinck, H., Couaillier, V., van der Ven, H., Sorensen, K.: ADIGMA–A European Initiative on the Development of Adaptive Higher-Order Variational Methods for Aerospace Applications: Results of a Collaborative Research Project Funded by the European Union, 2006–2009, vol. 113. Springer, Berlin (2010)
24. Kroll, N., Hirsch, C., Bassi, F., Johnston, C., Hillewaert, K.: IDIHOM: Industrialization of High-Order Methods-A Top-Down Approach: Results of a Collaborative Research Project Funded by the European Union, 2010–2014, vol. 128. Springer, Berlin (2015)
25. Lenormand, E., Sagaut, P., Ta Phuoc, L.: Large eddy simulation of subsonic and supersonic channel flow at moderate Reynolds number. Int. J. Numer. Methods Fluids **32**(4), 369–406 (2000)
26. Lesaint, P., Raviart, P.: On a Finite Element Method for Solving the Neutron Transport Equation. Academic, New York (1974)
27. Moser, R.D., Kim, J., Mansour, N.N.: Direct numerical simulation of turbulent channel flow up to Re_τ=590. Phys. Fluids **11**(4), 943 (1999)

28. Nguyen, N.C., Persson, P.O., Peraire, J.: RANS solutions using high order discontinuous Galerkin methods. AIAA Paper **914**, 2007 (2007)
29. Parsani, M., Bilka, M., Lacor, C.: Large eddy simulation of a muffler with the high-order spectral difference method. In: Spectral and High Order Methods for Partial Differential Equations-ICOSAHOM 2012, pp. 337–347. Springer, Heidelberg (2014)
30. Reed, W., Hill, T.: Triangular mesh methods for the neutron transport equation. Technical Report LA-UR-73-479, Los Alamos Scientific Laboratory (1973)
31. Roe, P.: Approximate Riemann solvers, parameter vectors, and difference schemes. J. Comput. Phys. **43**(2), 357–372 (1981)
32. Sengupta, K., Mashayek, F., Jacobs, G.: Large-eddy simulation using a discontinuous Galerkin spectral element method. In: 45th AIAA Aerospace Sciences Meeting and Exhibit (2007)
33. Wang, Z., Fidkowski, K., Abgrall, R., Bassi, F., Caraeni, D., Cary, A., Deconinck, H., Hartmann, R., Hillewaert, K., Huynh, H., Kroll, N., May, G., Persson, P.O., van Leer, B., Visbal, M.: High-order CFD methods: current status and perspective. Int. J. Numer. Methods Fluids **72**(8), 811–845 (2013)
34. Warburton, T., Lomtev, I., Kirby, R., Karniadakis, G.: A discontinuous Galerkin method for the Navier–Stokes equations on hybrid grids. Cent. Fluid Mech. **13**, 14 (1997)
35. Wei, L., Pollard, A.: Direct numerical simulation of compressible turbulent channel flows using the discontinuous Galerkin method. Comput. Fluids **47**(1), 85–100 (2011)